IEEE Access
Multidisciplinary | Rapid Review | Open Access Journal

Received 17 May 2026, accepted 6 June 2026, date of publication 16 June 2026, date of current version 23 June 2026.

Digital Object Identifier 10.1109/ACCESS.2026.3704070

RESEARCH ARTICLE

Superimposed Training Passive Time Reversal for Low SNR Communications

FÁBIO B. LOUZA[1] AND SÉRGIO M. JESUS[2], (Member, IEEE)
[1]Brazilian Navy Institute of Sea Studies Admiral Paulo Moreira (IEAPM), Arraial do Cabo 28930-000, Brazil
[2]LARSyS, University of Algarve, 8005-139 Faro, Portugal

Corresponding author: Fábio B. Louza (fabio.louza@marinha.mil.br)

This work was supported in part by the Postgraduate Study Abroad Program of Brazilian Navy under Grant Port.227/MB/2019, in part by the Project K2D–Knowledge and Data from the Deep Space funded by the Foundation for Science and Technology (FCT) Program MIT-Portugal under Contract 045941, in part by the BIOCOM Experiment funded by the National Council for Scientific and Technological Development (CNPq)/Science without Borders Program under Contract 401407/2014-4, and in part by the Article Processing Charge (APC) for the publication of this research funded by the Coordination for the Improvement of Higher Education Personnel–CAPES (ROR identifier: 00 × 0ma614).

ABSTRACT This paper presents a superimposed training passive time-reversal (STpTR) approach to deal with the passive time-reversal (pTR) environmental mismatch between the probe and the message transmissions. The probe is superimposed on the message and therefore, the probe and the message use the same sound channel. The proposed method uses a real-time Doppler-corrected probe to estimate the channel and perform pTR. The method compares 3 alternative strategies: the temporal diversity provided by repetitions of the same signal, the spatial diversity provided by two different geometry arrays of 4 hydrophones, and a combination of both with 8 hydrophones. STpTR mitigates multipath and performs error correction through coherent averaging. Residual intersymbol interference is removed by a Wiener filter. Results from a low signal-to-noise ratio (SNR) shallow-water experiment indicate the suitability of STpTR for both single and multichannel combining. STpTR combined with a Wiener filter provided an average mean-square error gain of up to 2.92 dB for single channels and 4.17 dB for multichannel combining, compared to a Wiener filter alone. The proposed method achieved a BER$< 10^{-2}$, for an in-band input SNR as low as -8 dB.

INDEX TERMS Low SNR communications, superimposed training, passive time-reversal, Wiener filter.

I. INTRODUCTION

In recent years, research on low signal-to-noise ratio (SNR) underwater acoustic communications has been encouraged by governments, industry, and academia due to its wide range of applications. In low SNR scenarios, the received signal power is comparable to or weaker than the ambient noise power within the communication frequency band. This severely limits the receiver's ability to distinguish the desired signal from background interference, leading to higher error rates, and degrading communication reliability. [1], [2], [3], [4], [5], [6]. Such conditions are common in shallow water due to impulsive biological sounds, vessel traffic, and multipath propagation that disperses energy over time. In practice, low SNR scenarios challenge reliable demodulation and synchronization because conventional detectors cannot easily distinguish the signal from noise. For covert or low-probability-of-detection (LPD) communications, researchers often define thresholds such as SNR < -8 dB [1], [7], where signals remain undetectable to unintended listeners yet must still be recoverable by specialized processing techniques.

The increasing deployment of battery-powered autonomous underwater vehicles (AUV) requires low power acoustic transmissions for command and control, extending operational autonomy [8], [9]. In military contexts, low SNR communications play a critical role in enabling covert operations, allowing underwater assets to remain undetected while maintaining connectivity [2], [4], [5], [8].

Low SNR conditions may occur naturally due to severe signal attenuation or high ambient noise levels in the

The associate editor coordinating the review of this manuscript and approving it for publication was Wei-Wen Hu.

underwater channel. However, deliberate transmission of low-power signals is often employed to meet operational constraints or strategic objectives. In addition, environmental concerns are also shaping the development of underwater communication systems. Several countries have implemented strict regulations to limit anthropogenic acoustic emissions in sensitive marine environments, demanding bio-friendly communications [1], [6].

Establishing coherent low SNR communications in shallow water is a challenging task [8], [9], [10]. Rapid fluctuation of the signal in time and space, long multipath delay spread, Doppler shift induced by sensors motion and sea surface, and high noise levels due to human and biological activities are factors that severely degrade low-power signal demodulation, motivating new signal processing techniques [1], [9], [10].

Passive time-reversal (pTR) techniques have been widely used to cope with multipath spread in shallow water [11], [12], [13], [14]. PTR usually relies on a spatio-temporal matched filter estimated by a probe sent before the data and requires a receiver array. In the absence of noise and assuming that both the sound channel structure affected by oceanographic features and the geometry between source and receiver remain unchanged, the received probes can be time-reversed and used to filter the message. To eliminate residual intersymbol interference (ISI), the pTR is usually followed by an adaptive filter, usually a decision feedback equalizer (DFE) with a phase-locked loop [14], [15], [16].

In the case of moving platforms and variable source-receiver geometries, especially in a fast time-varying ocean waveguide where the coherence time may be short, the classic approach of pTR sending the probe ahead of data may not be able to cope with the environmental mismatch between the probe and the message transmissions, even at high SNR [11], [13], [14]. Therefore, an environmental model-based time-reversal is proposed in [17]. The estimated noisy channel impulse responses (CIR) were replaced by time-updated and noiseless CIR replicas computed by a ray-tracing model. An extension of the pTR technique to adaptively weight receiver contributions to compensate for degraded focusing due to the geometrical mismatch between the probe and the data is presented in [13]. The interested reader is referred to [14] for an overview of time-reversal communications.

Most common state-of-the-art low SNR coherent-modulated communication systems are based on direct-sequence spread-spectrum (DSSS) [1], [2], [4], [7]. Symbols are spread by a code sequence, typically an M-sequence [18], resulting in a wideband signal. Considering that the spreading code is unknown to any unauthorized receiver accessing the communication network, a low probability of interception (LPI) is said to be achieved with DSSS modulation, transmitting at low power levels [4], [7]. However, there is an inevitable tradeoff between the data rate and the SNR. Operating at low data rates, DSSS takes advantage of frequency diversity and benefits from spreading gain in a low SNR environment to improve the performance of the communication system [4], [6]. In [7], two methods that use DSSS combined with pTR are presented for single receivers. The high SNR signals were recorded at sea and combined with ambient noise. Using a time-updated CIR as a matched filter, the methods achieved similar performance, yielding BER $< 10^{-2}$ at -12 dB input SNR. DSSS and a coherent RAKE receiver were also investigated to design spreading waveforms that can cope with the frequency-selective nature of the underwater channel, and also have interesting properties for LPD communications [4]. Adding AWGN to the data, the scheme achieved BER $< 10^{-2}$ for a SNR varying between -7 and -9 dB. The data rate was 156.25 bps. Another study on adaptive modulation for low SNR/covert communications based on a set of DSSS signals is presented in [2]. The authors proposed a DFE based on channel estimates and boosted trees for adaptive modulation. The data rate ranged from 13 to 116 bps. Combining the signals with AWGN to reduce the SNR in the receiver, BER lower than 10^{-2} were achieved using binary phase shift keying (BPSK) at -5 dB. In a work focused on bio-friendly communications, the authors presented a M-ary orthogonal code keying modulation (M-OCK) [6]. Based on recordings from a sea trial, with SNR adjusted by adding AWGN, the scheme achieved BER $< 10^{-3}$ for a $SNR = -14$ dB and data rate of 35.63 bps.

This paper proposes a receiver design to mitigate the environmental mismatch inherent in classical passive time-reversal (pTR). In conventional block-based pTR, the focusing filter relies on a preamble transmitted before the data payload. As a result, channel fluctuations and Doppler variations over the packet duration progressively degrade the accuracy of the estimate, reducing the multipath focusing. To address this limitation, the proposed superimposed training passive time-reversal (STpTR) scheme builds on the low-probability-of-detection framework [19] by embedding a continuous probe sequence directly into the data stream on a symbol-by-symbol basis.

The main novelty of this paper lies in integrating superimposed training with time-reversal processing. Unlike prior work [19], which applied superimposed training solely for single-hydrophone channel estimation and Wiener equalization, the proposed approach uses the instantaneous channel estimate to construct a pTR filter that coherently recombines multipath energy prior to equalization. Because the embedded probe and data are transmitted simultaneously through the same channel realization, this integration substantially reduces the temporal mismatch that limits classical block-based methods. The framework further incorporates Doppler compensation, multichannel array reception for spatial diversity, and Wiener post-filtering for residual ISI mitigation.

Although DFE is an established equalization benchmark, it is incompatible with the superimposed training structure adopted in this work. Its nonlinear feedback loop cancels postcursor ISI by treating the received signal as a pure data sequence, which disrupts the message-plus-probe superposition and prevents subsequent probe removal and

message retrieval. In contrast, the Wiener filter offers a robust, low-complexity alternative that is easier to implement, especially when paired with PTR to mitigate residual ISI in dynamic underwater environments. Therefore, a previous ST method based on a Wiener filter [19] is used as a reference. Performance is compared using STpTR, and STpTR as a pre-Wiener filter equalizer for in-band low SNR conditions ranging from –8 to 0 dB, representing a challenging operational regime for the proposed approach.

To demonstrate the concept in a low SNR scenario, this article uses a subset of data from the Biocom'19 shallow-water experiment, conducted off the coast of Cabo Frio/Brazil [20]. The sea-trial data were characterized by strong impulsive non-Gaussian noise. Instead of artificially degrading high-SNR recordings, low power transmissions were emitted from a single source and recorded by pyramidal and vertical linear arrays (VLA), each equipped with four hydrophones. The received signals were processed independently and combined. A larger and more spatially distributed configuration using all eight hydrophones was also investigated to assess the tradeoff between the overall robustness of the system and the number of receivers.

The paper is organized as follows. In Section II, the STpTR approach is presented. The shallow-water Biocom'19 experiment is described in Section III. The performance of STpTR communications is discussed in Section IV and conclusions are drawn in Section V. The list of symbols used in the article is given in Table 1.

TABLE 1. List of symbols used in the STpTR receiver.

Symbol	Definition
t	Continuous-time variable
k	Discrete-time index, $k = 1, \ldots, L$
$A[k]$	Superimposed training (ST) symbol sequence
$\tilde{s}(t)$	Continuous-time bandpass ST signal
$s(t)$	Continuous-time baseband ST signal
$s[k]$	Discrete-time baseband ST signal
z, Z	Repetition index and number of repetitions
m, M	Receiver index and number of receiver channels
τ_s	Symbol period
τ	Duration of one ST bitstream
$t' = t + z\tau$	Time variable for the z-th received bitstream
k'	Discrete-time sample index associated with t'
L	Length of the probe sequence
N	Degree of the M-sequence feedback equation
$x(t)$	Continuous-time probe (Mseq2047)
$x[k]$	Discrete-time probe (Mseq2047)
$d[k]$	Discrete-time message sequence
P	Probe amplitude
Q	Message amplitude
f_c	Carrier frequency
f_c'	Carrier frequency for Doppler-compensation
$\tilde{y}_z(t')$	Continuous-time received bandpass bitstream
$y_z(t')$	Continuous-time received baseband bitstream
$y_z[k']$	Discrete-time received baseband bitstream
$\widehat{y}[k']$	Recovered message after inverse FHT
$\mathbf{B}_{(16\times 2047)}$	Synchronous sampling matrix
$h_z[k]$	Channel impulse response (CIR)
$\widehat{h}_z[k]$	Estimated CIR
$o_z[k']$	STpTR output before equalization
$\widehat{q}_z[k']$	STpTR processor matched response
$w_z[n]$	Wiener equalizer coefficients
n	Wiener filter tap index
N_w	Wiener filter length
$g_{z,m}[k']$	Equalized output for repetition z and channel m
$r_{m,\mathrm{ave}}[k']$	Bitstream averaged over Z repetitions
$\check{r}_M[k']$	Bitstream averaged over M receiver channels
$p_{z,m}[k']$	FHT output used for soft synchronization
$\check{p}[k']$	FHT of $\check{r}_M[k']$ before HCC0
$\check{p}[k']$	$\check{p}[k']$ after HCC0
ρ_{xx}	Probe autocorrelation
ρ_{dx}	Message-probe crosscorrelation
η	HCC0 threshold
α	MAD scaling factor in $\eta = \alpha\,\mathrm{MAD}$
$\sigma^2_{Z,M}$	Average noise power
$\mathbf{R}_{oo}$	Autocorrelation matrix of $o_z[k']$
$\mathbf{r}_{xo}$	Crosscorrelation vector between $x[k]$ and $o_z[k']$
br_{eff}	Effective bit rate
$*$	Convolution
$\dagger$	Complex conjugate

II. SUPERIMPOSED TRAINING PASSIVE TIME-REVERSAL

A. SUPERIMPOSED TRAINING BITSTREAM

The STpTR concept involves summing a long probe to the message before transmission using the same symbol rate. The sketch in Fig. 1 shows the superimposed training (ST) bitstream. The probe $x[k]$ is a binary phase-coded maximum length sequence, known as M-sequence (Mseq2047) [18], where $k = 1, 2, \ldots, L$ is a discrete time-index, $L = 2^N - 1$ is the length of the probe sequence, and $N = 11$ is the degree of the feedback equation. Pseudorandom and deterministic, M-sequences present a noise-like spectrum and have good autocorrelation properties, being commonly used to estimate the impulse response of the ocean waveguide. Furthermore, as codes are orthogonal, multiple users may access the channel with a low degree of interference [21]. The message sequence $d[k]$ is composed of three padding bits followed by four consecutive streams of 511 bits, where the 480-bit data packets are delimited by short M-sequences of 31 bits (Mseq31). The padding bits are needed to conform the message length to the standard 2047-bit probe length.

The ST bitstream symbol sequence $A[k] = Px[k] + Qd[k]$, where P and Q are the probe and the message amplitudes, $x[k] \in \{-1, +1\}$ is the probe code, and $d[k] \in \{-1, +1\}$ is the message. The probe and the message may differ in both amplitude and phase. The optimal value of the amplitude ratio Q/P is governed by a two-sided trade-off. For $Q/P \ll 1$, the probe dominates the transmitted waveform, yielding accurate CIR estimation but sacrificing data recovery at the receiver. Furthermore, high probe energy levels raise detectability for an interceptor employing energy detection. In contrast, for $Q/P \gg 1$, the data dominates and the probe becomes too weak to reliably estimate the CIR, degrading time-reversal focusing. In this work, an intermediate value $Q/P = 4/5$ is employed, such that the probe amplitude exceeds that of the message, corresponding to a message-to-probe ratio of -1.94 dB. By retaining the phase of the probe, the ST bitstream achieves a high pulse-compression gain, improving both channel estimation and pTR demodulation. Furthermore, as the message is embedded in the training sequence, the ST bitstream closely approximates a noise-like waveform, making the embedded message difficult

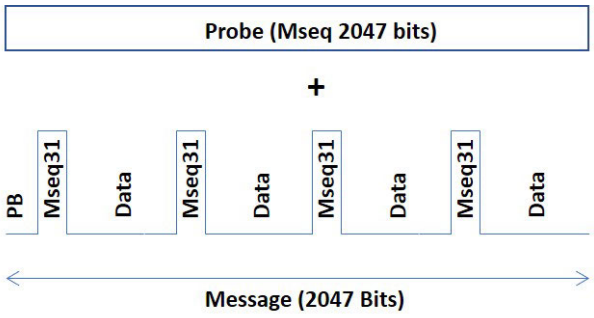

FIGURE 1. Superimposed training bitstream is created by summing the probe (Mseq2047) and the message. The message has three padding bits (PB) and four data packets of the same content (480 bits), preceded by a short Mseq31 for hard synchronization.

to extract without prior knowledge of the probe code, thus exhibiting low probability of detection/interception (LPD/LPI) properties.

The BPSK-modulated baseband bitstream $s(t)$ is given by $s(t) = \sum_{k=0}^{L-1} A[k]q(t - k\tau_s)$, where $q(t)$ is a rectangular pulse shape of duration τ_s, and τ_s is the symbol period. The transmitted bandpass binary signal $\tilde{s}(t)$ is given by

$$\tilde{s}(t) = \Re\left\{s(t)e^{j2\pi f_c t}\right\} \tag{1}$$

where f_c is the carrier frequency. The same low-power $\tilde{s}(t)$ of period $\tau = 4L/f_c$ is repeated several times and recorded by multiple receivers. In this work, all four 480-bit data packets have the same content. The redundancy of signals in both time and space allows error correction and multichannel gain through coherent averaging. As the method explores repetition coding, the effective bit rate can be expressed as $br_{eff} = [480f_c]/[4LZ]$, where f_c is the carrier frequency, L is the probe sequence length, and Z is the number of repetitions used for coherent averaging.

The following subsections discuss the receiver structure according to the block diagram in Fig. 2. Fig. 2(a) shows the STpTR, channel equalization, soft synchronization in time, and coherent averaging of Z low power bitstreams. Fig. 2(b) shows the multichannel combining, hyperslice cancellation by coordinate zeroing (HCC0), hard synchronization, and message retrieval.

B. DETECTION AND DOPPLER COMPENSATION

In a reverberating channel or in the presence of relative motion between the source and the receiver, the Doppler frequency spread/shift of transmitted binary probes must be compensated for to improve detection and synchronization [10], [14]. Considering $t' = t + z\tau$ as the time slot of the z-th sequence, each received bandpass bitstream $\tilde{y}_z(t')$ is correlated with a bank of matched filters formed from Doppler-shifted replicas of the probe signal $\tilde{x}(t)_{f_c'}$ calculated for candidate carrier frequencies f_c' that account for source/receiver motion. The resulting Doppler index ($I_{Dop_{f_c'}}$) is based on the maximum absolute value of the correlation

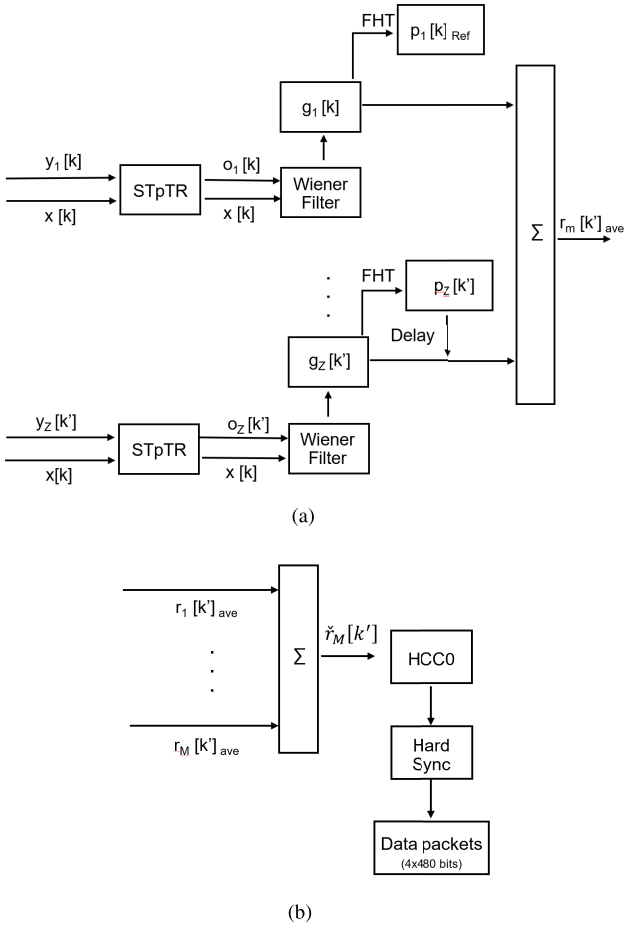

FIGURE 2. a) Diagram of STpTR, channel equalization, soft synchronization in time, and coherent averaging of Z low power bitstreams; b) Diagram of multichannel combining, HCC0, hard synchronization, and message retrieval.

given by

$$I_{Dop_{f_c'}} = max[|\tilde{y}_z(t') * \tilde{x}^{\dagger}(-t)_{f_c'}|] \tag{2}$$

where $\tilde{x}^{\dagger}(-t)_{f_c'}$ is the bandpass time-reversed frequency-shifted probe replica known to the receiver. Here and throughout this paper, $*$ and $\dagger$ stand for convolution, and complex conjugate.

The bitstream $\tilde{y}_z(t')$ is then resampled for the f_c', corresponding to the highest $I_{Dop_{f_c'}}$, significantly improving detection. After Doppler compensation, $\tilde{y}_z(t')$ is converted from bandpass to baseband, synchronous sampling to form matrix $B_{(16\times 2047)}$.

Fig. 3 (left) shows that each bit modulates 4 cycles of the carrier wave. The sampling frequency $f_s = 4f_c$. Fig. 3 (right) shows that each row of matrix B is filled with the corresponding sample of each bit. Thus, the first row of B is given by $[s_1, s_{17}, \ldots, s_{32735}]$, and similarly for the remaining rows. The rearrangement in matrix B shows that the odd rows have samples close to zero and even rows fluctuate in amplitude but reverse the probe phase in 180°, where $B(2, k) \simeq -B(4, k) \simeq B(6, k) \simeq \ldots \simeq -B(16, k)$ for $k = 1 \ldots 2047$.

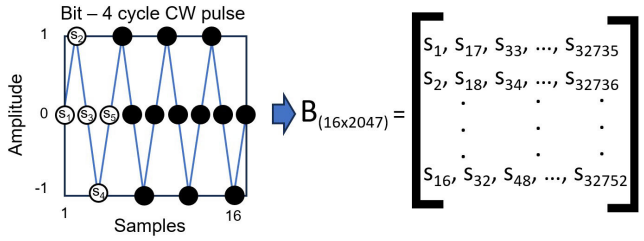

FIGURE 3. Left) One bit modulates 4 cycles of the carrier wave, sampled four times f_c. Right) Matrix $B_{(16\times2047)}$ is formed by synchronous sampling the bitstream.

After reversing the sign (phase) of rows 4, 8, 12, and 16, all even rows are summed, sample by sample. This produces a single 2047-sample discrete-time baseband sequence $y_z[k]$ containing most of the energy of the original bandpass bitstream.

C. STpTR IN TIME, WIENER EQUALIZATION AND TEMPORAL SOFT SYNCHRONIZATION

The block diagram in Fig. 2(a) describes the STpTR processing, Wiener equalization, and temporal soft synchronization. In a noiseless and time-invariant channel, the received signal can be modeled as $y_z[k] = s[k] * h_z[k]$, where $s[k]$ is the transmitted bitstream and $h_z[k]$ is the channel impulse response (CIR). Because shallow-water acoustic waveguides are inherently noisy and rapidly time-varying, the ST framework assumes the channel is quasi-stationary only over the short duration of a single bitstream. By linearly superimposing the probe $x[k]$ and the message payload, both signals experience the same instantaneous channel realization. This co-transmission mitigates the temporal mismatch that typically degrades conventional preamble-based pTR, where the CIR estimate may become outdated as the channel evolves between probe transmission and payload reception, leading to mismatch in the time-reversal operator and reduced multipath focusing. In contrast, ST allows the receiver to extract a temporally aligned CIR estimate from the same received bitstream used for detection, keeping the time-reversal operator close to the matched condition. However, because the probe and message occupy the same time-frequency space, the unknown data symbols act as self-interference during channel estimation. Consequently, STpTR accepts a higher initial CIR estimation noise, governed by the data-to-probe power ratio Q/P, in exchange for improved robustness against rapid channel fading.

Let k' denote the corresponding discrete-time index of t' after synchronous sampling. The noisy, interference-corrupted CIR estimate $\widehat{h}_z[k'] = y_z[k'] * x^{\dagger}[-k]$ is computed efficiently via the Fast Hadamard Transform (FHT), as described in Section II-G. For each sensor, the STpTR functions as a matched filter convolving the received bitstream $y_z[k']$ with the time-reversed CIR $\widehat{h}_z[-k']$ (3).

$$o_z[k'] = y_z[k'] * \widehat{h}_z^{\dagger}[-k'] = s[k] * \underbrace{\left[h_z[k'] * \widehat{h}_z^{\dagger}[-k']\right]}_{\widehat{q}_z[k']} \quad (3)$$

where $\widehat{q}_z[k'] = h_z[k'] * \widehat{h}_z^{\dagger}[-k']$ is the effective matched response of the STpTR processor. When the CIR estimate is temporally aligned with the data channel, $\widehat{h}_z[k'] \approx h_z[k']$, $\widehat{q}_z[k']$ approaches an impulse, maximising temporal focusing. Channel mismatch broadens $\widehat{q}_z[k']$, reduces its main-lobe amplitude, and increases sidelobe energy, directly raising the residual ISI floor at $o_z[k']$. To prevent the message-induced estimation error and ambient noise from dominating the matched-filter output, the CIR estimate $\widehat{h}_z[-k']$ is time-gated to include only the energetic main arrivals. The result is the focusing of the weak pulse energy after multipath recombination. However, there is always a residual ISI, which requires equalization to be mitigated [10], [14].

In this paper, the STpTR is followed by a Wiener filter equalizer [22], [23], an optimal filter under the minimum MSE criterion. Assuming that the system is LTI over the duration of each received bitstream and that signals are wide-sense stationary over this interval, the Wiener filter coefficients $w_z[n]$ are estimated through the Wiener–Hopf equation so as to minimize the MSE between the filter output $g_z[k']$ and the training signal $x[k]$, where

$$g_z[k'] = \sum_{n=0}^{N_w-1} w_z[n]\, o_z[k'-n], \quad (4)$$

and N_w denotes the filter length. In matrix form, the Wiener–Hopf solution is given by $\mathbf{w_z} = \mathbf{R}_{oo}^{-1}\mathbf{r}_{xo}$, where $\mathbf{R}_{oo}$ is the autocorrelation matrix of the time-reversal output signal $o_z[k']$, and $\mathbf{r}_{xo}$ is the crosscorrelation vector between $x[k]$ and $o_z[k']$.

For each channel m, the consecutive $g_{z,m}[k']$ are time-aligned using the strongest peak of the corresponding FHT $p_{z,m}[k']$), where $p_{1ref,m}[k']$ is taken as the reference. After soft synchronization, the coherent averaging of Z repetitions provides a processing gain of approximately $10\log_{10}(Z)$ dB, resulting in a high SNR bitstream $r_{m,\text{ave}}[k']$ (5).

$$\begin{aligned} r_{m,\text{ave}}[k'] &= \frac{1}{Z}\sum_{z=1}^{Z} g_{z,m}[k'] \\ &= s[k'] * \left[\frac{1}{Z}\sum_{z=1}^{Z} w_{z,m}[n] * \widehat{q}_{z,m}^{\dagger}[-k']\right] \end{aligned} \quad (5)$$

As shown in Sec. IV-D and IV-E, increasing the number of averaging sequences (Z) improves the effective SNR of $r_{m,\text{ave}}[k']$, reducing the bit error rate (BER) and thereby improving the communication system performance.

D. STpTR, AND SOFT SYNCHRONIZATION IN SPACE

The $r_{m,\text{ave}}[k']$ is calculated for all M elements of the array (Fig. 2(b)). The spatial synchronization is similar to that performed in time. The output of the STpTR $\check{r}_M[k']$ is obtained after coherent averaging of all M channels (6).

$$\check{r}_M[k'] = \frac{1}{M}\sum_{m=1}^{M} r_{m,\text{ave}}[k']$$

$$= s[k'] * \left[\frac{1}{MZ} \sum_{m=1}^{M} \sum_{z=1}^{Z} w_{z,m}[n] * \widehat{q}^{\dagger}_{z,m}[-k'] \right] \quad (6)$$

where the bracketed term may be interpreted as the Q-function [11], [24], modified by the Wiener coefficients.

The Q-function is defined as the summation of $q_z[k']$ across the receiver array [14], [24]. The main lobe contributions from different sensors add coherently in phase, while the secondary lobes are misaligned in delay and phase and therefore do not reinforce each other. Temporal focusing is quantified by the peak-to-sidelobe (PSL) ratio, which depends on factors such as the multipath structure, the number of receivers and their spatial distribution. Furthermore, PSL ratio is highly sensitive to the input SNR [14], [24]. At low SNR, noise corrupts the channel estimation, weakening the main signal peak and reducing the sharpness of the focus. A high noise floor may also mask the secondary lobes, making it difficult to distinguish the signal from background interference. As the SNR increases through coherent averaging of all M channels, the Q-function becomes progressively sharper, approaching a delta-like response. This improved focusing facilitates synchronization and decoding, thereby enhancing the performance of the STpTR method.

To illustrate the effect of spatial and temporal diversity, the PSL is expressed as PSL $\propto \frac{MZ}{\sigma^2_{Z,M}}$, where MZ represents the coherent combining gain provided by time-reversal processing [14], and $\sigma^2_{Z,M}$ denotes the average noise power. This expression is not intended as a rigorous theoretical bound, but rather as a qualitative description of the PSL trend under the ambient-noise conditions observed in the BioCom'19 experiment.

E. PROBE INTERFERENCE CANCELLATION

The time/space averaged bitstream $\check{r}_M[k']$ still contains the probe superimposed on the message. To remove this co-channel interference, a process called Hyperslice Cancellation by Coordinate Zeroing (HCC0) is performed [19], [21], [25]. Before HCC0, a FHT over $\check{r}_M[k']$ compresses the probe energy into a few samples (7).

$$\check{p}[k'] = \check{r}_M[k'] * x^{\dagger}[-k'] \quad (7)$$

Let $s[k']$ denote the discrete-time baseband ST sequence associated with $A[k']$, as defined in Sec. II-A. By substituting (6) into (7) and expanding $s[k']$ in terms of the probe and message contributions, it can be seen that the correlation output contains two main components: (i) a desired term proportional to $P\rho_{xx}$, associated with the autocorrelation of the probe code, and (ii) an interference term proportional to $Q\rho_{dx}$, associated with the crosscorrelation between the message and the probe, treated here as additive noise (8).

$$\check{p}[k'] = [P\rho_{xx} + Q\rho_{dx}] * \ldots \\ \ldots * \left[\frac{1}{MZ} \sum_{m=1}^{M} \sum_{z=1}^{Z} w_{z,m}[n] * \widehat{q}^{\dagger}_{z,m}[-k'] \right] \quad (8)$$

Fig. 4(a) shows the soft synchronization before HCC0 of a transmitted bitstream during the BioCom'19 experiment (Sec. III). The equalized term involving ρ_{xx} (black circle) is removed by zeroing out the samples having amplitude higher than a threshold η (dashed line), defined using the Median Absolute Deviation (MAD) of the ambient noise (9).

$$\check{p}[k'] = \begin{cases} 0, & \text{if } |\check{p}[k']| > \eta \\ \check{p}[k'], & \text{elsewhere} \end{cases}, \text{for } 0 \le t' \le \tau. \quad (9)$$

As shown in Figs. 6 and 7, ambient noise in the $6-9$ kHz band is predominantly generated by snapping shrimp. Their acoustic emissions are highly impulsive and broadband, resulting in a heavy-tailed, non-Gaussian amplitude distribution [26], for which MAD provides a robust measure of dispersion less affected by outliers than variance. The detection threshold was therefore defined as $\eta = \alpha \cdot \text{MAD}$, where α regulates the trade-off between probe suppression and message preservation. Small values of α may lead to unintended removal of message-bearing components, misclassifying moderate shrimp impulses as probe-related samples. Conversely, large values of α may leave residual probe interference after cancellation, thereby degrading message recovery. The interval $3 \le \alpha \le 5$ was selected to reflect the impulsive-noise conditions observed at the BioCom'19 site, marked by variable snapping shrimp activity and low SNR. This formulation enhances the robustness of the cancellation process to spatial and temporal variations in the noise statistics. After HCC0, an inverse FHT (IFHT) is applied to the remaining sequence $\check{p}[k']$ to recover the message $\widehat{y}[k']$.

F. HARD SYNCHRONIZATION AND MESSAGE RETRIEVAL

Hard synchronization is performed using cross-correlation peaks from FHT of Mseq31 that precede data packets (Fig. 4(b)). After synchronization (black circles), the receiver retrieves the four 480-bit payloads.

G. COMPUTATIONAL ANALYSIS OF EQUALIZERS

In this work, due to the superimposed training scheme, the STpTR cross-correlations are performed using the Fast Hadamard Transform (FHT), also called the Fast M-Sequence Transform, which is briefly described in Appendix A. The FHT exploits a permutational equivalence between Sylvester–Hadamard and M-sequence matrices to reduce the correlation complexity to $O(L \log_2 L)$, where L is the probe length. Furthermore, the FHT is implemented through a butterfly structure consisting only of additions and subtractions, thereby avoiding floating-point multiplications within the transform stage. In contrast, the stability and performance of the Wiener filter are strongly influenced by the conditioning of $\mathbf{R}_{oo}$, whose construction and inversion scale as $O(N_w^2)$ or $O(N_w^3)$ depending on the chosen solver, where N_w is the number of filter taps required to represent the channel multipath. As a pre-equalizer, STpTR reduces the channel delay spread and, consequently, the computational

burden of the matrix-solution stage, as a smaller N_w is required [22].

III. SHALLOW WATER BioCom'19 EXPERIMENT

The BioCom'19 experiment was conducted at a shallow-water site, in Cabo Frio Island Bay (Brazil), from January 14 to 18, 2019. Described in detail in [20], the experiment focused on monitoring biological soundscape and underwater communications. It was performed near the city harbor and along the rocky shores, an area with substantial coverage of soniferous invertebrates [27], adding natural impulsive broadband noise to the received signals. Furthermore, the experimental site is influenced by the upwelling phenomena in the region of Cabo Frio Island. Rapid changes in ocean temperature stratification affect sound wave propagation [28], making this a challenging site for underwater communication experiments by combining severe multipath propagation with nonstationary sound-speed structures that degrade synchronization and symbol detection.

Communication signals were set with a central frequency f_c of 7.5 kHz, and a bandwidth of 3 kHz. Fig. 5(a) shows the experimental setup. The omnidirectional acoustic source was located mid-water in a 4 m deep water column, approximately 1.6 km away from the receiver location. In the nautical chart (Fig. 5(b) (left)), one can observe that the bathymetry changes drastically along the propagation path. Through a bottom depression between the source and receivers, strong currents flow in and out of the test site modifying both the temperature and sound speed profiles, creating a highly range-dependent channel. To perform error correction through coherent averaging, the bitstream was transmitted 55 times per minute at five-minute intervals. Because all four data packets carry identical content, this scheme constitutes repetition coding. In this framework, the number of processed signals Z governs the latency-throughput trade-off: values of $Z = 4$, 10, and 20 yield effective bit rates (br_{eff}) of 110, 44, and 22 bps, respectively, with higher Z improving resistance to fading at the expense of reduced throughput.

Data were recorded on two different geometry arrays of 4 hydrophones each. The vertical linear array (VLA) with a 4.5 m aperture was deployed in an 8 m water column to sample the channel's vertical energy structure. The triangular pyramidal array with a 1 m-long edge, was posed at the bottom, approximately 2.8 m from the VLA location. The data acquisition system has a sampling frequency of 52734Hz, but signals were downsampled to 30KHz, 4 times f_c, and Doppler compensated before processing. The hydrophones have a sensitivity of -174.9 dB re 1V/1μPa and a flat frequency response between 0.1 and 40 kHz.

IV. STpTR COMMUNICATION PERFORMANCE

A small subset of data from BioCom'19, recorded on January 17, 2019, between 1:10 p.m. and 2:30 p.m., using both the linear and pyramidal arrays, was employed to test the STpTR concept. Fig. 5(b) (right) shows the SSP measured during the same period at the source/receiver locations, along with the bottom depression at the bay entrance. The slightly downward refracting sound speed profiles indicate that sensors close to the bottom may receive more acoustic energy compared to those placed along the water column. The reader is referred to [29] where the energy propagation and the CIR during the experiment were studied using both an acoustic model and real data.

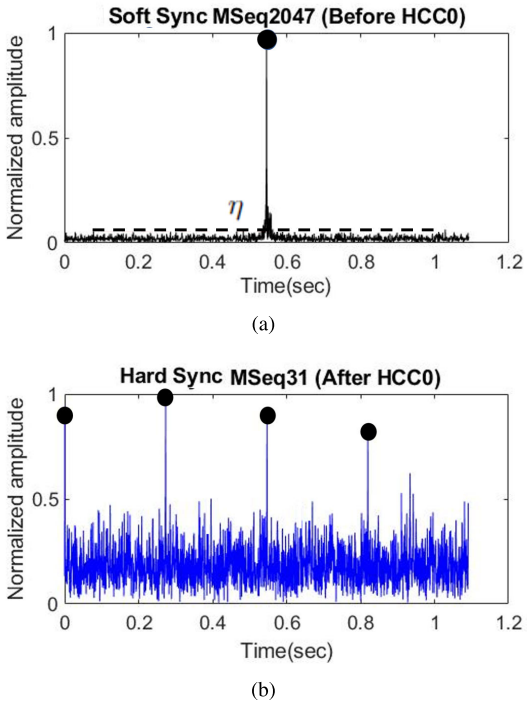

FIGURE 4. a) Soft synchronization prior to HCC0. A FHT over $\check{r}_M[k']$ concentrates probe energy (black circle). HCC0 cancels probe interference ρ_{xx} by zeroing samples above the threshold η (dashed line). b) Hard synchronization after HCC0, based on a FHT of MSeq31 (black circles), reveals the four data packets.

A. AMBIENT NOISE AND SNR ESTIMATION

To evaluate the performance of the proposed communication system in a low SNR environment, it is important to take into account both the level and the statistics of the ambient noise, and the power of the transmitted signals. Figs. 6 and 7 (left) show the ambient noise recorded on Jan 17, 2019, at 1:15 p.m. by channel #1 of the pyramidal array, positioned near the bottom, and by channel #4 of the VLA, located closer to the surface. In shallow water, the dominant noise contribution in the 6–9 kHz band, corresponding to the frequency range of the proposed communication system, comes from the activity of the snapping shrimp, which is known for its strong impulsive nature [26].

The corresponding normal probability plots are presented in the middle panels of Figs. 6 and 7. This statistical tool evaluates how closely a dataset follows a Gaussian distribution: perfect agreement results in data points forming a straight line. However, both plots exhibit an S-shaped curve,

reflecting heavier tails than a Gaussian distribution. This indicates that large-amplitude events occur more frequently than expected, a signature of impulsive noise superimposed on background Gaussian fluctuations. Such deviations from linearity reveal a non-Gaussian noise distribution, an unfavorable noise statistics that can intermittently mask or distort the useful arrivals, degrading the performance of linear correlators used for detection and synchronization [26].

Figs. 6 and 7 (right) show a non-constant in-band noise power spectrum density (PSD) for all four channels of both pyramidal and vertical linear arrays. To allow for a better comparison of the noise behaviour along frequency, a shift from channel #1 of −10 dB (channel #2), −20 dB (channel #3), and −30 dB (channel #4) was applied over the original PSD values. There is a difference in the signal amplification used in each array expressed by the recorded amplitudes (Figs. 6 and 7 (left)), and by the in-band PSD (Figs. 6 and 7 (right)). Despite a similar noise spectrum between hydrophones from the same array, the power varies slightly. This fact is clearer for the VLA, where channel #4 is almost superimposed on channel #3, despite the 10 dB difference, indicating a higher noise level closer to the surface. This depth-dependent noise exposure is a known characteristic of shallow-water environments and underscores that array geometry and receiver depth are not merely geometric parameters as they affect the local SNR budget available to each element.

In this work, all 55 bitstreams in each block were transmitted using the same source power level pre-defined according to the time of the transmission. The signal power was kept constant during the first 30 minutes of each hour, and reduced by 1 dB after each 5-minute block transmission, in the remaining 30 minutes. Each SNR estimate was computed over the Z bitstreams transmitted at the same power level, ensuring a consistent statistical basis for comparison. The combination of intentional power variation and the naturally high variability of the impulsive noise environment yielded a broad SNR range across the dataset, enabling a meaningful evaluation of system performance across operating conditions that are representative of real shallow-water deployments.

The in-band SNR (dB) for each channel m was estimated according to $SNR_m = 10log_{10}\left(\frac{S_m - N_m}{N_m}\right)$, where S is the mean of the signal plus noise power of Z sequences, N is the mean of the noise power of a sequence of the same length as S, estimated from a period after transmission. For multichannel combining, the average input SNR of the array was estimated as $SNR_{array} = 10log_{10}\left[\frac{1}{M}\sum_{m=1}^{M}\left(\frac{S_m - N_m}{N_m}\right)\right]$, where M is the number of channels. Note that SNR_{array} is defined here as an empirical descriptor of the average input SNR across the array aperture, rather than a formal theoretical bound.

B. DOPPLER ANALYSIS

Fig. 8 shows the Doppler shift estimated from bitstreams recorded on Jan 17, 2019, at 1:15 p.m., by the 4 sensors from both arrays. Although the source and receivers were

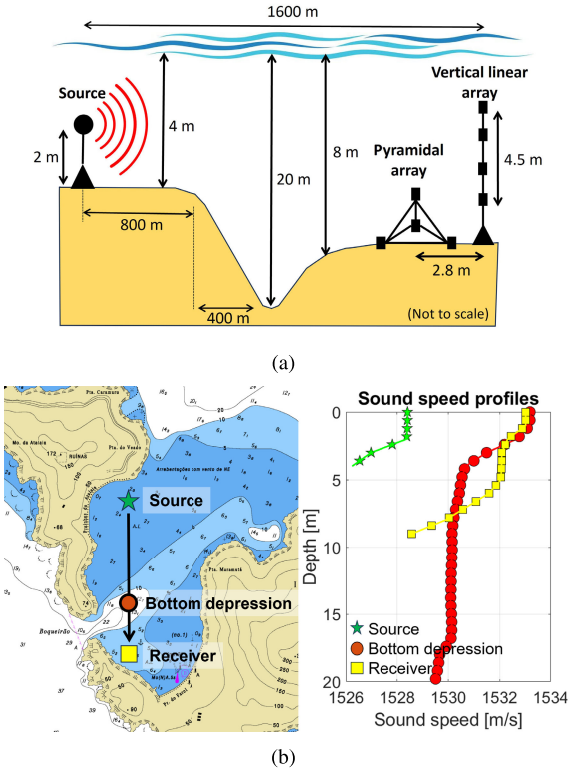

FIGURE 5. a) Experimental setup of the BioCom'19 experiment (not to scale). b) Left: Nautical chart indicates the propagation track. Right: Sound speed profiles acquired on Jan 17, 2019 between 1:10 p.m and 2:30 p.m, at the source (green pentagram), bottom depression (red circle), and receiver (yellow square) locations.

nominally steady, the observed shifts arose primarily from oceanographic dynamics and buoy agitation, indicating that motion-induced frequency offsets remain relevant even in fixed configurations. To compensate for these effects, a bank of matched filters was employed. Centered on $f_c = 7.5$ kHz, the bank was configured with a frequency resolution of 0.5 Hz over 11 discrete bins, covering a Doppler range of approximately ±2.5 Hz, corresponding to a maximum relative speed of 1 knot observed during the experiment. This design ensured sensitivity to small-scale motion typical of coastal acoustic environments.

For the pyramidal array (PA), Fig. 8 (left) shows shifts ranging from −1.9 Hz to +1.6 Hz, with an average standard deviation (σ_{PA}) of 0.9 Hz across the 4 channels. The source, anchored and suspended on a subsurface buoy close to shore experienced small, random displacements driven by wave action and vessel wakes. Thus, although the receiving hydrophones were fixed, the observed variability in σ_{PA} captures the combined effects of this source motion, dynamic surface scattering, and local currents. For the vertical linear array (VLA), Fig. 8 (right) shows shifts from −2.2 to +2.4 Hz, with a larger average standard deviation ($\sigma_{VLA} = 1.4\ Hz$). Hydrophones moved randomly around their equilibrium positions, with sensor #4 (farther from

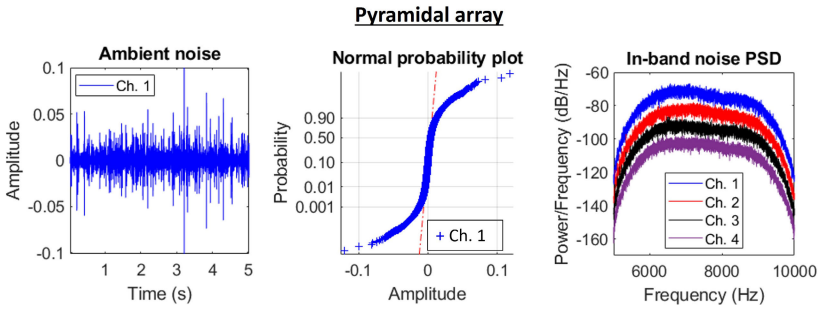

FIGURE 6. Noise statistics for channel #1 of the pyramidal array. Left: Impulsive ambient noise recorded on Jan 17, 2019, at 1:15 p.m. Middle: Normal probability plot shows a noise distribution deviation from linearity suggesting a non-Gaussian distribution. Right: In-band noise power spectrum density (PSD) for all four channels. A shift from channel #1 of −10 dB (channel #2), −20 dB (channel #3), and −30 dB (channel #4) shows a similar frequency distribution and acoustic power.

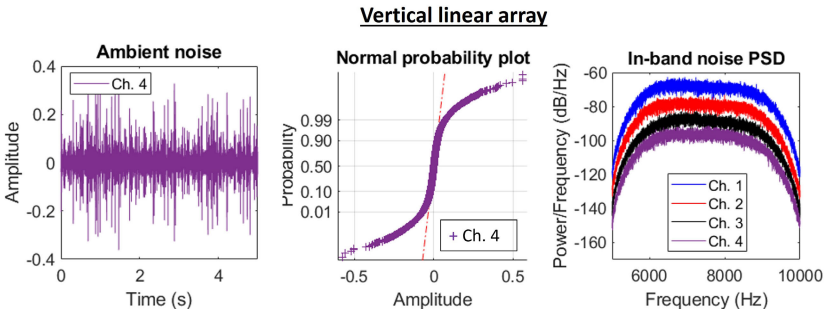

FIGURE 7. Noise statistics for channel #4 of the vertical linear array. Left: Impulsive ambient noise recorded on Jan 17, 2019, at 1:15 p.m. Middle: Normal probability plot shows a noise distribution deviation from linearity suggesting a non-Gaussian distribution. Right: In-band noise power spectrum density (PSD) for all four channels. A shift from channel #1 of −10 dB (channel #2), −20 dB (channel #3), and −30 dB (channel #4) shows a similar frequency distribution but a slightly noisier channel #4.

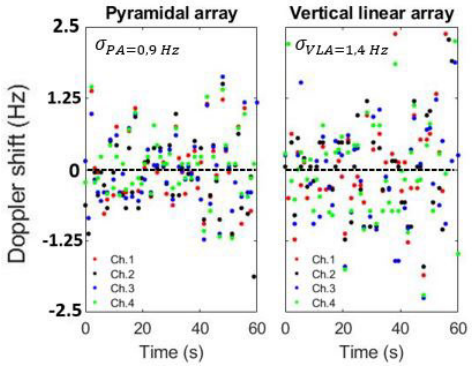

FIGURE 8. Estimated Doppler shifts across the four channels of the pyramidal and vertical linear arrays, extracted from 55 bitstreams recorded on January 17, 2019, at 1:15 p.m. The pyramidal array (PA) displays lower variability ($\sigma_{PA} = 0.9$ Hz) compared to the vertical linear array (VLA) ($\sigma_{VLA} = 1.4$ Hz), consistent with the greater sensitivity of vertically extended geometries to motion-induced platform instability.

the anchor) showing greater displacement than sensor #1 near the bottom. The simultaneous motion of both source and sensors amplified Doppler variability compared to the PA due to the greater mechanical excursion along the water column. This comparison between both arrays illustrates that even nominally stationary shallow-water deployments exhibit Doppler fluctuations that must be explicitly addressed in system design.

C. DETECTION OF LOW SNR SIGNALS

Fig. 9 shows the matched-filter (MF) outputs for comparison of the 55 consecutive Doppler compensated bitstreams (Jan 27, 2019 - 1:15 p.m.). The correlation results for each channel were normalized to the maximum peak of each array. Fig. 9 (upper row) shows that the hydrophones of the pyramidal array, separated by approximately 5 wavelengths at $f_c = 7.5$ kHz, recorded uncorrelated signals. The SSP points to a stable propagation region close to the bottom, which evenly ensonifies the hydrophones. In contrast, Fig. 9 (lower row) presents the matched-filter outputs for the VLA hydrophones. Placed along the water column, VLA element spacing is 7.5 wavelengths at f_c, providing a wider spatial diversity compared to the smaller pyramidal array. The VLA sensor #1 closer to the bottom received more acoustic energy and presented stronger correlation peaks, compared to sensor #4, closer to the sea surface. This depth-dependent

difference is consistent with the downward-refracting sound-speed structure, which concentrates energy toward the lower portion of the water column. The VLA correlation peaks exhibit more aggressive time-varying fading compared to those of the pyramidal array. Between 55 and 60 seconds, most bitstreams were barely detected by all hydrophones due to a source power level reduction. Amplitude fluctuations of the dominant correlation peaks, across both time and space, confirm the difficulty of reliable detection in shallow-water channels. Even under stable conditions, fading and source-level variations can intermittently suppress signal detectability. These observations highlight the importance of diversity-based processing strategies for maintaining performance at low SNR.

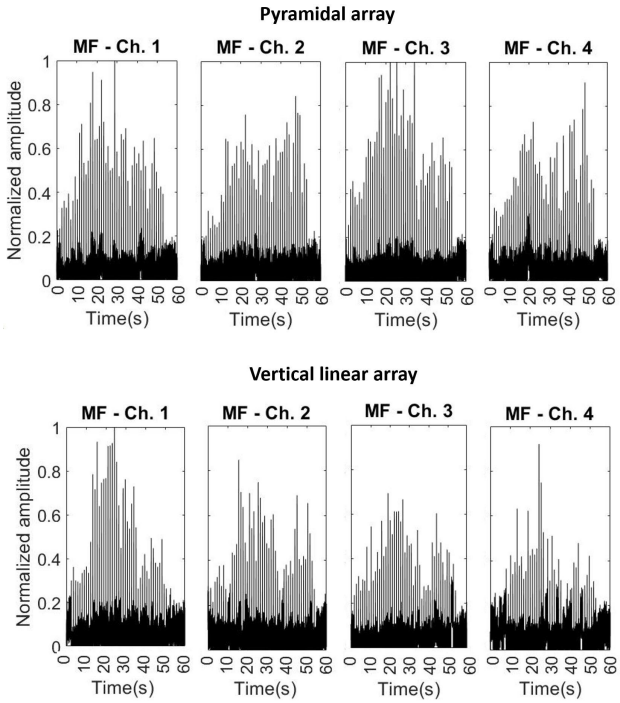

FIGURE 9. Matched filter (MF) outputs from 55 Doppler compensated bitstreams (Jan 17, 2019, 1:15 p.m.). Upper row: pyramidal array channels showing relatively stable correlation. Lower row: VLA channels exhibiting stronger fading and variability across channels. The stronger correlation peaks in the lower VLA sensor and pyramidal array channels reflect the energy concentration near the bottom under the measured downward-refracting conditions.

In covert communication scenarios, spectral analysis becomes a necessary energy detection strategy because an interceptor lacks access to the codes required for matched-filter detection [1]. Fig. 10 presents a spectrogram of low-SNR signals recorded by channel #1 of the pyramidal array. Three SNR intervals illustrate detectability under varying conditions. In timeframe 1 (0–22 s), the signal is barely visible ($SNR_{ave} = -6.22$ dB). In timeframe 2 (23–57 s), the average SNR increased to -0.36 dB, making the broadband transmission visible. Timeframe 3 (58–70 s) corresponds to a noise-only period after transmissions ceased. These fluctuations, likely driven by channel fading, show that detectability depends not only on average signal level but also on short-term channel stability. Spectral methods therefore provide a complementary perspective on signal presence, particularly under degraded or covert communication conditions.

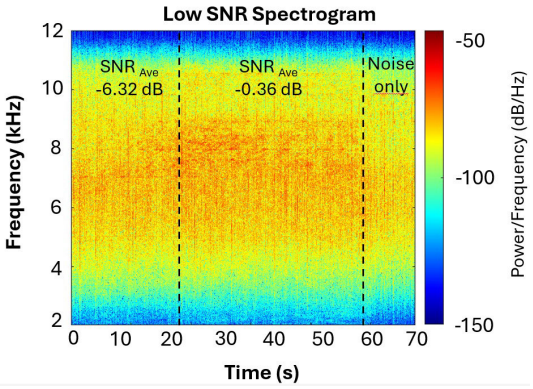

FIGURE 10. Spectrogram of low SNR signal recorded by channel #1 of pyramidal array on Jan 17, 2019, at 1:15 p.m. Timeframe 1 (0 to 22s): signal is barely visible ($SNR_{Ave} = -6.22$ *dB*); Timeframe 2 (23 to 57s): signal is visible ($SNR_{Ave} = -0.36$ *dB*); Timeframe 3 (58 to 70s): noise-only period.

D. STpTR FOR A SINGLE RECEIVER

Fig. 11 presents the estimated CIR, STpTR pulse compression, and Q function using the first 5 Doppler-compensated bitstreams (BT) recorded by two representative sensors on Jan 17, 2019 - 1:15 p.m. Fig. 11 (upper row, left) details the multipath structure of the normalized and time-aligned CIR estimated from hydrophone #1 placed at the top of the pyramidal array. Located approximately 1 m above the bottom, the CIR present multiple strong arrivals and short multipath. Fig. 11 (lower row, left) shows the CIR estimated from hydrophone #4 of the VLA, placed approximately 2.5 m below the sea surface. The CIR present a delay spread longer than 15 ms, including energetic late arrivals that may complicate the synchronization and equalization processes.

Before implementing the matched-filter, the estimated CIR $\widehat{h}_z[-k']$ in (3) was time-gated to 20 ms to include only the main arrivals and mitigate noise interference. Fig. 11 (middle) demonstrates the ability of STpTR to overcome these harsh conditions and perform the multipath recombination for each sequence, independently. The sharpness of the resulting focus depends on the multipath structure as can be compared in Fig. 11 for sensor #1 of the pyramidal array (upper row, middle) and sensor #4 of the VLA (lower row, middle). The remaining sidelobes are related to the residual ISI. Thus, STpTR is followed by a Wiener filter equalizer. By setting the Wiener coefficients in (5) to unity, STpTR is analyzed for a single sensor (M=1) from each array, enabling comparison of the Q-function under different propagation conditions.

The Q-function in time is obtained by summing the five previously matched-filtered sequences. In this process, the main lobes of the autocorrelation functions combine coherently, whereas the sidelobes tend to interfere destructively. The Q-function therefore provides a compact indicator

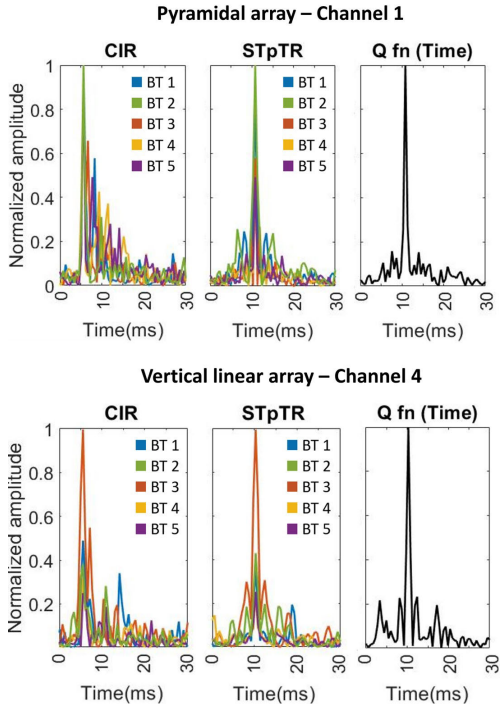

FIGURE 11. Channel impulse responses (left), STpTR multipath recombination (middle), and the corresponding Q-function evaluated over time (right) for the first five bitstreams recorded on Jan 17, 2019, at 1:15 p.m. Results are shown for channel #1 of the pyramidal array (upper row) and channel #4 of the vertical linear array (lower row). The Q-function panels illustrate the quality of spatio-temporal focusing, where a dominant mainlobe and suppressed sidelobes indicate effective multipath compression and mitigation of inter-symbol interference (ISI).

of how effectively temporal focusing suppresses residual intersymbol interference (ISI) under different propagation conditions. As shown in Fig. 11 (upper row, right), sensor #1 of the pyramidal array achieves a peak-to-sidelobe (PSL) ratio of 8.2 dB, while sensor #4 of the VLA exhibits a lower PSL ratio of 6.1 dB. The higher and more temporally spread sidelobes in the channel #4 indicate that the benefit of STpTR is strongly dependent on the structure of the channel. In more dispersive channels, time-reversal focusing alone leaves stronger residual interference after recombination. The comparison of Q-functions is not only descriptive, but diagnostic, indicating when temporal focusing is sufficient and when an additional equalization stage becomes necessary. Increasing the number of averaged bitstreams improves the PSL and reduces residual ISI by exploiting repetition coding, but this gain is achieved at the expense of a lower effective bit rate (br_{eff}). Therefore, in a single-receiver low-SNR setting, robustness is obtained through a direct tradeoff between throughput and redundancy.

A common benchmark for high-SNR acoustic communications, the decision-feedback equalizer (DFE), has also been applied in low-SNR scenarios [2]. However, because DFE relies on decision-directed feedback, it is not suitable for the present superimposed training framework, in which hard decisions can disturb the embedded message.

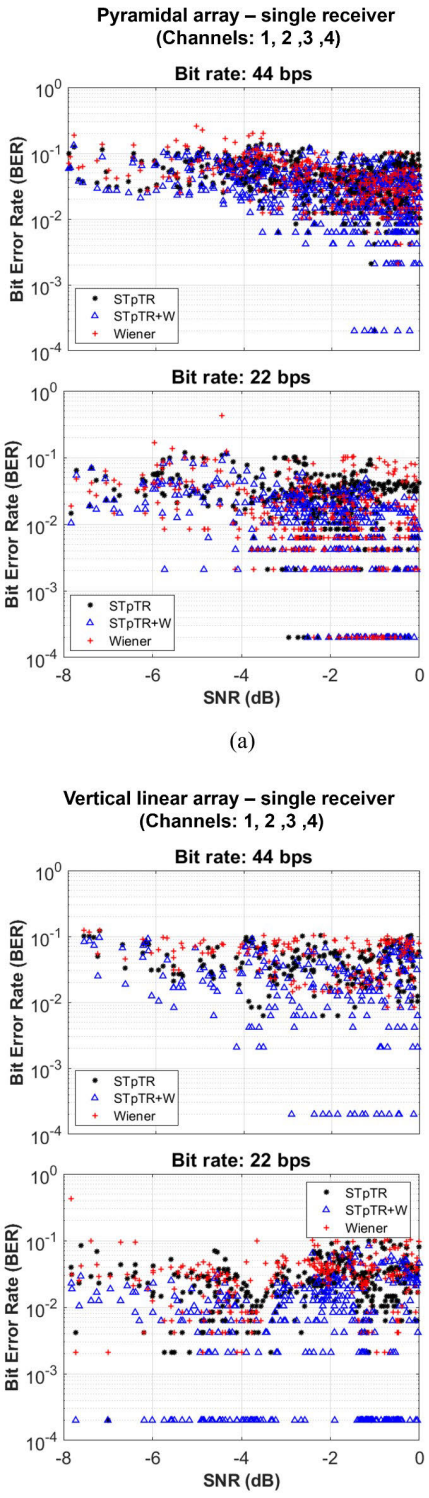

FIGURE 12. Single-channel BER versus input SNR for STpTR+W (blue triangles), STpTR (black dots), and the Wiener filter benchmark (red crosses) across individual receivers of the (a) pyramidal array and (b) vertical linear array. Top panels represent an effective bit rate of $br_{\text{eff}} = 44$ bps (10.9 s averaging), while bottom panels show $br_{\text{eff}} = 22$ bps (21.8 s averaging). Zero BER is plotted at 2×10^{-4} on the logarithmic scale. While STpTR alone generally underperforms the Wiener filter, the combined STpTR+W approach consistently reverses this trend across all cases.

For this reason, the minimum-MSE Wiener filter is adopted here as the reference equalizer [19]. This choice serves not only to benchmark equalizer performance, but also to isolate the role of STpTR as a linear channel-conditioning stage preceding symbol estimation. Two filtering strategies are evaluated: STpTR alone, and STpTR followed by a Wiener filter (STpTR+W). To emulate single-receiver platforms, such as autonomous underwater vehicles or network nodes operating at different ranges and depths, the bitstreams received by each hydrophone were processed independently. To enhance processing gain and enable error correction, the bitstreams were coherently averaged over durations of 10.9 and 21.8 seconds (10 and 20 bitstreams), yielding effective bit rates (br_{eff}) of 44 and 22 bps, respectively.

Fig. 12 shows the BER versus SNR performance for single receivers (channels 1-4) of the pyramidal and VLA over an input SNR range of -8 to 0 dB. At $br_{\text{eff}} = 44$ bps, the BER curves remain limited and only weakly monotonic with SNR, indicating that averaging over 10 bitstreams is often insufficient to overcome the combined effects of fading, impulsive noise, and channel estimation uncertainty. This regime reveals that, in low SNR shallow-water channels, performance is not determined by average SNR alone, but also by the extent to which temporal averaging can stabilize the focusing process. In contrast, at $br_{\text{eff}} = 22$ bps, the additional temporal redundancy produces more consistent gains, higher PSL values, improved temporal compression, and a larger fraction of error-free transmissions. Across most cases, the combined STpTR followed by Wiener equalization (STpTR+W, blue triangles) outperforms both STpTR alone (black stars) and Wiener filtering alone (red crosses). This behavior supports the interpretation of STpTR as a pre-equalization stage. By compressing the effective multipath prior to adaptive filtering, it reduces channel dispersion, shortens the required Wiener filter, and improves the conditioning of the Wiener-Hopf problem. In a few transmissions, Wiener filtering alone performs comparably or better, which is consistent with channels that already exhibit short delay spread and therefore require little or no prefocusing. Thus, the advantage of STpTR should be understood as channel dependent, with the strongest gains arising in the more dispersive and unstable propagation conditions.

Table 2 presents the average mean squared error (MSE) gain achieved by the proposed equalization methods relative to the Wiener filter benchmark [19]. The MSE, expressed in decibels, is defined as $MSE_{dB}(\hat{d}) = 10\log_{10}(MSE(\hat{d}))$, where $MSE(\hat{d}) = \frac{\sum(d-\hat{d})^2}{480}$. Here, d and $\hat{d}$ represent the transmitted and estimated data symbols, respectively. The MSE gains (Δ) of STpTR and STpTR+W are calculated as the difference between the Wiener filter MSE and that of the corresponding equalizer: $\Delta\text{MSE}_{\text{STpTR(dB)}} = MSE_{W_{dB}}(\hat{d}) - MSE_{STpTR_{dB}}(\hat{d})$ and $\Delta\text{MSE}_{\text{STpTR+W(dB)}} = MSE_{W_{dB}}(\hat{d}) - MSE_{STpTR+W_{dB}}(\hat{d})$. STpTR alone generally underperforms the Wiener filter under both array configurations, as indicated by negative $\Delta\text{MSE}_{\text{STpTR(dB)}}$ values and higher BERs. In contrast, the combined STpTR+W approach reverses this trend, producing positive $\Delta\text{MSE}_{\text{STpTR+W(dB)}}$ values and significant BER reductions relative to the Wiener benchmark. For the pyramidal array, $BER_{STpTR+W}$ is reduced by 25.5% and 12.7% at 44 and 22 bps, respectively. The vertical linear array follows a similar pattern but with sharper contrasts, yielding reductions of 27.5% and 48.9% relative to BER_W, representing the largest observed gain.

TABLE 2. Average MSE gain (Δ) compared to the Wiener filter (single channel).

Array	Pyramidal		VLA	
Bit rate br_{eff} (bps)	44	22	44	22
STpTR+W (dB)	1.28	0.59	1.44	2.92
STpTR (dB)	−0.04	−1.85	−0.55	−0.15

The single-receiver analysis demonstrates that STpTR is most effective not as a complete equalization strategy, but as a channel-conditioning stage that improves the robustness of subsequent Wiener filtering. Furthermore, the differences in sensor performance are determined by local channel physics and temporal averaging limits. These results motivate the use of spatial diversity via multichannel combining, as discussed in Section IV-E.

E. STpTR FOR MULTIPLE RECEIVERS

To investigate spatio-temporal multichannel combining, this study evaluates three array configurations: the pyramidal and vertical linear arrays individually (each employing four hydrophones), and their joint use as an eight-hydrophone system. By coherently averaging signals across multiple sensors, the Q-function sidelobes are attenuated, which mitigates intersymbol interference. This spatial diversity introduces a processing gain that supports higher effective bit rates (br_{eff}), thereby reducing the reliance on temporal averaging. To quantify the tradeoff between spatial and temporal diversity, received bitstreams were averaged over approximately 4.4 and 10.9 seconds (corresponding to 4 and 10 bitstreams) for $br_{eff} = 110$ and 44 bps, respectively.

The results in Figs. 13(a)-(b) illustrate how multichannel combining changes the role of STpTR compared to the single-receiver case. Once spatial diversity is exploited, system performance depends not only on temporal averaging but also on the array's ability to capture independent realizations of the multipath field. In effect, spatial combining introduces a processing gain that can partially replace temporal redundancy, thereby supporting higher effective bit rates without compromising robustness. The pyramidal array and the VLA achieve comparable BER performance after multichannel combining for both $br_{eff} = 110$ and 44 bps. This similarity is informative because the two arrays probe the channel differently as the pyramidal array samples a compact region near the bottom, while the VLA samples the vertical structure of the field. The fact that both geometries yield similar outcomes underscores that array performance

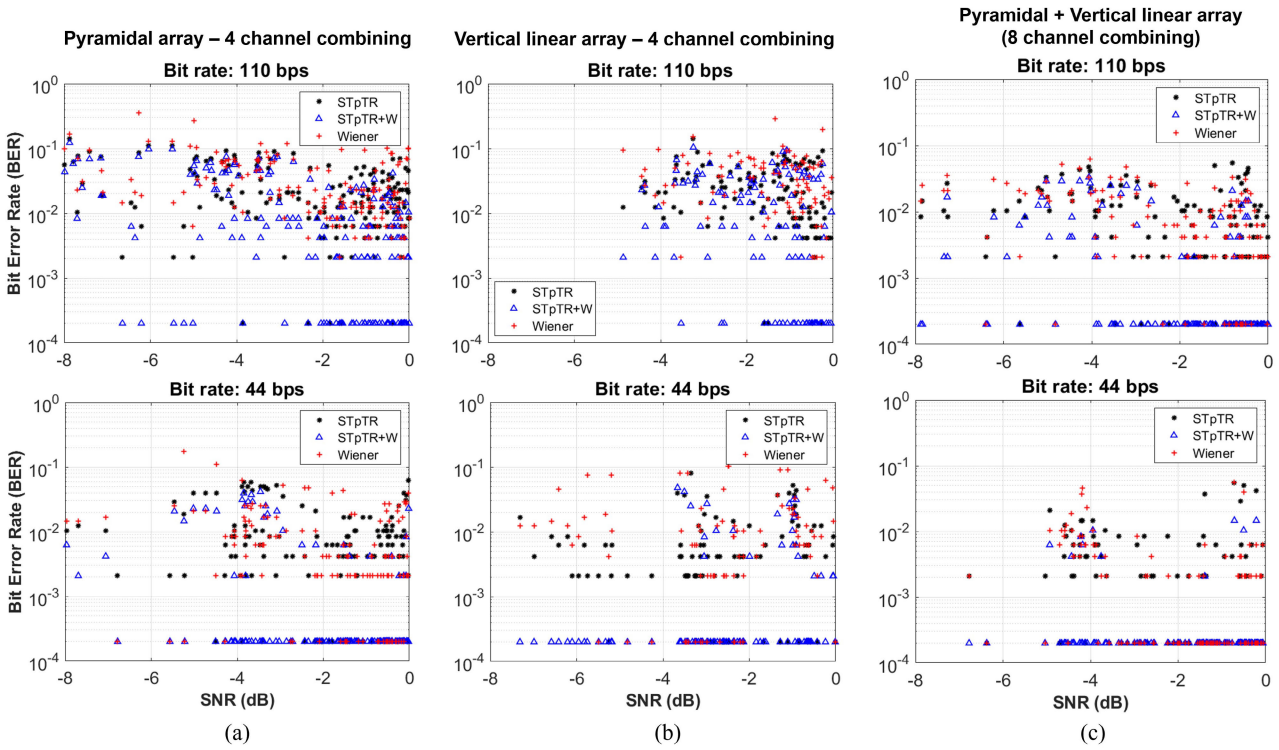

FIGURE 13. BER versus SNR for STpTR+W (blue triangles), STpTR (black dots), and Wiener filtering (red crosses) after multichannel combining for the pyramidal array (a), vertical linear array (VLA) (b), and pyramidal+VLA (c). Zero BER is represented by 2×10^{-4} on the logarithmic scale. Top panels (a–c): $br_{eff} = 110$ bps, averaging 4.4 seconds. Bottom panels (a–c): $br_{eff} = 44$ bps, averaging 10.9 seconds. Under multichannel combining, the spatial diversity effectively substitutes for temporal redundancy, allowing STpTR alone to outperform the Wiener filter at higher bit rates. The combined STpTR+W approach yields the most robust erformance, achieving significant BER reductions relative to the Wiener benchmark, particularly as the number of distributed receivers increases.

is influenced less by geometry itself than by how effectively sensors intercept stable and energetic arrivals under prevailing channel conditions. Although several bitstreams from VLA sensors #3 and #4 were discarded, likely due to downward refraction reducing signal energy at the upper sensors, the combined VLA still achieved BER $< 10^{-2}$ throughout most of the -8 to 0 dB input-SNR range. With the STpTR+W equalizer, more than 32% of messages at $br_{eff} = 110$ bps and 59% at $br_{eff} = 44$ bps were decoded without errors, demonstrating that spatial combining substantially reduces the burden otherwise imposed on temporal averaging alone.

The combined pyramidal+VLA configuration in Fig. 13(c) highlights the system-level consequence of increasing the number of receivers. By joining two arrays separated by 2.8 m, the receiver samples a broader spatial region and captures a more diverse set of arrivals than either four-hydrophone configuration alone. This increase in spatial diversity reduces Q-function sidelobes, mitigates residual ISI, and improves decoding robustness across bit rates and equalizers. The proportion of error-free messages rises by more than 40% compared to the performance of the individual arrays, showing that distributed reception provides gains that cannot be reproduced by temporal averaging alone. More broadly, the benefit of multichannel combining is structural rather than additive, since wider spatial sampling reshapes the effective channel experienced by the receiver and makes STpTR-based processing substantially more reliable.

TABLE 3. Average MSE gain (Δ) compared to the Wiener filter (multichannel combining).

Array	Pyramidal		VLA		Pyram.+VLA	
Bit rate br_{eff} (bps)	110	44	110	44	110	44
STpTR+W (dB)	3.08	1.31	4.17	2.53	2.18	0.63
STpTR (dB)	0.44	−1.61	2.14	0.81	0.14	1.14

Table 3 summarizes the average mean-squared-error (MSE) gains of STpTR and STpTR+W relative to the Wiener benchmark under multichannel combining. The benefit of STpTR becomes more pronounced as the effective bit rate increases and the number of temporally averaged bitstreams decreases. At $br_{\text{eff}} = 110$ bps, STpTR alone already outperforms the Wiener filter in all array configurations, indicating that spatial diversity can compensate for reduced temporal redundancy at higher rates. When followed by Wiener filtering, STpTR achieves substantial BER reductions of 50.7%, 61.7%, and 39.5% for the pyramidal, VLA, and pyramidal+VLA configurations, respectively, with the greatest relative gain observed for the VLA. At $br_{\text{eff}} = 44$ bps, STpTR continues to outperform the Wiener filter,

although the additional benefit of STpTR+W becomes more moderate because temporal averaging already provides part of the required robustness. The combined receiver remains the best overall performer, with BER reductions of 26.9%, 44.1%, and 13.5% relative to Wiener filtering alone.

Taken together, the multichannel results support a broader interpretation of STpTR than in the single-receiver case. STpTR alone provides limited and channel-dependent gains when only temporal diversity is available, but becomes substantially more effective once spatial diversity is exploited. In that regime, STpTR is no longer just a prefocusing stage for a subsequent equalizer but becomes an integral part of a spatio-temporal equalization strategy whose effectiveness grows as the receiver samples a larger and more diverse portion of the channel. The consistent superiority of STpTR+W across array configurations and bit rates therefore suggests that the combined architecture is especially attractive for shallow-water links where temporal averaging is constrained but spatial sampling can be increased.

V. CONCLUSION

This paper presents an alternative approach for dealing with the environmental mismatch between the probe and the data transmissions, in passive time-reversal applications for underwater communications. Based on superimposed training low-power signals, the method uses a Doppler corrected real-time probe to estimate the channel and mitigate multipath distortions over data. After STpTR, the residual ISI is treated by the Wiener filter equalizer. The Biocom'19 shallow water experiment proved the concept for single and multichannel receivers. The results show that STpTR may help to reduce acoustic pollution using low-power signals and can be further explored for covert communications. Due to the double synchronization, based on coded sequences known only to legitimate receivers, the method may be said to provide low probability of detection/interception (LPD/LPI), protecting the privacy of communications. The low SNR, varying between -8 and 0 dB, combined with the aggressive fading in time and space have impacted the equalization performance. The method explored both temporal and spatial diversity to increase the SNR and to perform error correction through coherent averaging. Separated by just a few wavelengths, the hydrophones from the pyramidal array observed the channel from almost the same depth. Their combination provided a higher processing gain than those of the VLA, positioned along the water column. This fact may be related to the downward refracting SSP profile in the shallow water waveguide, which favored higher signal energy in the deeper part of the channel. To understand the tradeoff between the number of averaged sequences and the number of receivers, BER vs. SNR was estimated for different effective bit rates and sensors configuration. Both 4-hydrophone arrays and a more complex 8-hydrophone array achieved BER $< 10^{-2}$, including several error-free messages. When operating independently, the STpTR achieved performance comparable to that of the Wiener filter, but at a substantially lower computational cost, with an execution time approximately four times shorter. The greatest performance gains, however, were obtained when STpTR was employed as a pre-equalization stage. In this configuration, the proposed STpTR+Wiener scheme provided an average MSE gain, $\Delta\text{MSE}_{\text{STpTR+W}_{\text{dB}}}$, of up to 2.92 dB for single-channel processing and 4.17 dB for multichannel combining. By compressing the channel impulse response prior to Wiener equalization, the STpTR stage improved communication reliability i) reducing BER at fixed bit rates, and ii) enabling higher effective bit rates by requiring fewer averaged bitstreams. These findings highlight the potential of STpTR-assisted Wiener filtering as a practical solution for robust, low-power, and covert underwater communications in challenging shallow-water environments.

APPENDIX A
EFFICIENT CORRELATION USING FAST HADAMARD TRANSFORM

The conventional approach to performing cross-correlation of a received baseband bitstream $y[k]$ with the M-sequence probe $x[k]$, known to the receiver, is shown in (10)

$$h[k] = y[k] * x^{\dagger}[-k], \tag{10}$$

where h denotes the channel impulse response, and $\dagger$ denotes complex conjugate.

Let us assume $y[k]$ is sampled once per symbol. For $t = l(1 \leq l \leq L)$, the discrete-time sequence $y[l]$ may be represented by the vector $\mathbf{y}_{L\times 1}$. Therefore, in matrix form, (10) may be rewritten as

$$\mathbf{h}_{L\times 1} = \mathbf{X}_L \mathbf{y}_{L\times 1}, \tag{11}$$

where $\mathbf{X}_L$ is the M-sequence probe square matrix and L is the probe period. However, instead of performing a direct multiplication, the fast Walsh−Hadamard transform of M-sequences, also called fast M-Sequence transform [18], exploits the permutational equivalence between the M-sequence ($\mathbf{X}_L$) and the Sylvester−Hadamard matrices ($\mathbf{H}_{L+1}$). Thus, the matrix multiplication by the Walsh−Hadamard matrix may proceed via a butterfly algorithm similar to the fast Fourier transform (FFT) [30]. Replacing multiplications of direct correlation by addition and subtraction operations only, the correlation number of operations is drastically reduced from L^2 to $Llog_2L$ saving substantial computational time.

A. THE M-SEQUENCE MATRIX

Maximal length sequence, known as M-sequence [18], [30], is a binary sequence generated by a linear feedback shift register whose primitive polynomial of degree N is given by

$$f(x) = x^N + \sum_{i=0}^{N-1} c_i x_i \tag{12}$$

The resulting pseudorandom M-sequence vector $[\mathbf{x}_k] = [c_1, \ldots c_{2^N-1}]$ can be shown to have an impulse-like autocorrelation function, and for this reason, is commonly used

in communication systems for multiple purposes (channel estimation, synchronization...). The cyclic permutations of the code may generate an orthogonal square M-sequence matrix $\mathbf{X}_{2^N-1}$ of order $L = 2^N - 1$. The first row of $\mathbf{X}_L$ is $[\mathbf{x}_k]$ and the successive rows are cyclic shifts of $[\mathbf{x}_k]$. For a given value of N, there exist several M-sequences but those created from a large N present better correlation properties. Let us consider, for example, the M-sequence code $[\mathbf{x}_k] = [1, 1, 1, 0, 0, 1, 0]$, created from the recursive equation $f(x) = x^3 + x + 1$. The corresponding M-sequence matrix of order L, where N=3, is given by

$$\mathbf{X}_L = \begin{bmatrix} 1 & 1 & 1 & 0 & 0 & 1 & 0 \\ 1 & 1 & 0 & 0 & 1 & 0 & 1 \\ 1 & 0 & 0 & 1 & 0 & 1 & 1 \\ 0 & 0 & 1 & 0 & 1 & 1 & 1 \\ 0 & 1 & 0 & 1 & 1 & 1 & 0 \\ 1 & 0 & 1 & 1 & 1 & 0 & 0 \\ 0 & 1 & 1 & 1 & 0 & 0 & 1 \end{bmatrix} \tag{13}$$

B. THE HADAMARD MATRIX

A Sylvester-Hadamard matrix $\mathbf{H}_{2^N}$ [18], [30] is defined as a square matrix of order $L + 1 = 2^N$ where all entries are ± 1 and its row vectors define a complete set of orthogonal functions. Thus, $\mathbf{H}_{L+1}\mathbf{H}_{L+1}^\top = (L+1)\mathbf{I}_{L+1}$, where $\mathbf{H}^\top$ is the transpose of $\mathbf{H}_{L+1}$, and $\mathbf{I}_{L+1}$ is the identity matrix. The Hadamard matrix exists only for a power of 2 and may be computed recursively as

$$\mathbf{H}_{L+1} = \mathbf{H}_{2^N} = \begin{bmatrix} \mathbf{H}_{2^{N-1}} & \mathbf{H}_{2^{N-1}} \\ \mathbf{H}_{2^{N-1}} & -\mathbf{H}_{2^{N-1}} \end{bmatrix}, \tag{14}$$

for $N \geq 1$, where $\mathbf{H}_1 = [1]$.

Thus, for N=3

$$\mathbf{H}_8 = \begin{bmatrix} +1 & +1 & +1 & +1 & +1 & +1 & +1 & +1 \\ +1 & -1 & +1 & -1 & +1 & -1 & +1 & -1 \\ +1 & +1 & -1 & -1 & +1 & +1 & -1 & -1 \\ +1 & -1 & -1 & +1 & +1 & -1 & -1 & +1 \\ +1 & +1 & +1 & +1 & -1 & -1 & -1 & -1 \\ +1 & -1 & +1 & -1 & -1 & +1 & -1 & +1 \\ +1 & +1 & -1 & -1 & -1 & -1 & +1 & +1 \\ +1 & -1 & -1 & +1 & -1 & +1 & +1 & -1 \end{bmatrix} \tag{15}$$

C. EFFICIENT CYCLIC CORRELATION USING FHT

The computation algorithm of the FHT to perform the cyclic correlation of M-sequences is described in this section. The equivalence between the M-sequence and the Hadamard matrices may be shown through the equivalence of their factors over the Galois Field (2) (GF(2)), where the elements are represented by 0's and 1's [18], [25].

The M-sequence matrix (13) may be decomposed as a linear modulo-2 combinations of the first N rows/columns of $\mathbf{X}_L$ as (16):

$$\mathbf{X}_L = \mathbf{G}_{L\times N}\mathbf{V}_{L\times N}^\top = \begin{bmatrix} 1 & 0 & 0 \\ 0 & 1 & 0 \\ 0 & 0 & 1 \\ 1 & 1 & 0 \\ 0 & 1 & 1 \\ 1 & 1 & 1 \\ 1 & 0 & 1 \end{bmatrix} \cdot \begin{bmatrix} 1 & 1 & 1 \\ 1 & 1 & 0 \\ 1 & 0 & 0 \\ 0 & 0 & 1 \\ 0 & 1 & 0 \\ 1 & 0 & 1 \\ 0 & 1 & 1 \end{bmatrix}^\top \tag{16}$$

where $\mathbf{G}_{L\times N}$ consists of columns in $\mathbf{X}_L$ which the first N rows form an identity matrix, and $\mathbf{V}_{L\times N}^\top$ is the transpose matrix of the first N rows of $\mathbf{X}_L$.

The Hadamard matrix (15) is converted from the reals to the GF(2), denoted by $\tilde{\mathbf{H}}_{L+1}$, replacing 1's by 0's and -1's by 1's. Thus, $\tilde{\mathbf{H}}_{L+1}$ may be factored as given by (17):

$$\mathbf{H}_{L+1} = \mathbf{B}_{L+1\times N}\mathbf{B}_{L+1\times N}^\top \tag{17}$$

where $\mathbf{B}_{L+1\times N}^\top = \begin{bmatrix} 0 & 0 & 0 & 0 & 1 & 1 & 1 & 1 \\ 0 & 0 & 1 & 1 & 0 & 0 & 1 & 1 \\ 0 & 1 & 0 & 1 & 0 & 1 & 0 & 1 \end{bmatrix}$.

The permutational equivalence between the M-sequence and the Hadamard matrices may be observed bordering the matrix $\mathbf{G}_{L\times N}$ on top with a row of all 0's, and the matrix $\mathbf{V}_{N\times L}$ on the left with a column of all 0's. The resulting $\hat{\mathbf{G}}_{L+1\times N}$ and $\mathbf{B}_{L+1\times N}$ differ by a row permutation, while $\hat{\mathbf{V}}_{N\times L+1}$ and $\mathbf{B}_{L+1\times N}^\top$ differ by a column permutation.

But $\hat{\mathbf{G}} = \mathbf{P}_G\mathbf{B}$ and $\hat{\mathbf{V}} = \mathbf{B}^\top\mathbf{P}_V$, where $\mathbf{P}_G$ and $\mathbf{P}_V$ are permutation square matrices of size $(L+1)$. Thus, the M-sequence matrix $\mathbf{X}_L$ may be rewritten as (18)

$$\begin{aligned} \mathbf{X}_L &= \mathbf{Z}_R\mathbf{P}_G\mathbf{B}\mathbf{B}^T\mathbf{P}_V\mathbf{Z}_I \\ &= \mathbf{Z}_R\mathbf{P}_G\mathbf{H}_{L+1}\mathbf{P}_V\mathbf{Z}_I \end{aligned} \tag{18}$$

where $\mathbf{Z}_{I_{(L+1\times L)}} = \begin{bmatrix} 0 \\ I_L \end{bmatrix}$ is used to increase the size of the received bitstream y_L from L to L+1, $\mathbf{I}_L$ is the identity matrix and $\mathbf{Z}_{R_{(L\times L+1)}} = \begin{bmatrix} 0 & I_L \end{bmatrix}$ is a matrix to reduce the size of the channel impulse response (CIR) vector from L+1 to L. The correlation equivalence described above, despite being constructed under GF (2), is implemented under the reals, replacing 0's for 1's, and 1's for -1's. But the matrices $\mathbf{P}_V$ and $\mathbf{P}_G$ may work in both GF(2) and reals domains.

Therefore, the correlation in (11) may be performed using the fast Hadamard transform (18): i) increasing the size of the received bitstream y_L to L+1 using $\mathbf{Z}_{I_{(L+1\times L)}}$ and reordering the data according to $\mathbf{P}_V$; ii) multiplicating by the Walsh-Hadamard matrix via a butterfly algorithm similar to the FFT [30]; iii) reordering the transformed data according to $\mathbf{P}_G$ and reducing the size from L+1 to L.

D. THE INVERSE FHT

The inverse FHT (IFHT) (19) is also efficiently performed, similarly to the FHT in (11).

$$\mathbf{y}_{L\times 1} = \mathbf{X}_L^{-1}\mathbf{h}_{L\times 1} \tag{19}$$

As the inverses of $\mathbf{P}_G$ and $\mathbf{P}_V$ in (18) are their transpose, IFHT may use the same mapping matrices as follows

$$\mathbf{X}_L^{-1} = \mathbf{Z}_I^T\mathbf{P}_G^T(\mathbf{H}_{L+1})^{-1}\mathbf{P}_V^T\mathbf{Z}_R^T \tag{20}$$

Using the butterfly algorithm, similar to the IFFT, the IFHT avoids the calculation of the inverse of a large matrix of size L. The interested reader is referred to [18], [25], and [30] for further details.

ACKNOWLEDGMENT

The authors would like to thank Brazilian Navy Institute of Sea Studies Admiral Paulo Moreira for the support of the experiment at sea.

REFERENCES

[1] R. Diamant and L. Lampe, "Low probability of detection for underwater acoustic communication: A review," *IEEE Access*, vol. 6, pp. 19099–19112, 2018.
[2] K. Pelekanakis and L. Cazzanti, "On adaptive modulation for low SNR underwater acoustic communications," in *Proc. OCEANS MTS/IEEE Charleston*, Oct. 2018, pp. 1–6.
[3] F. Schulz and T. Wiegand, "Underwater acoustic communications for submarines–A sonar company's perspective," in *Proc. 4th Underwater Commun. Netw. Conf. (UComms)*, Aug. 2018, pp. 1–5.
[4] J. Ling, H. He, J. Li, W. Roberts, and P. Stoica, "Covert underwater acoustic communications," *J. Acoust. Soc. Amer.*, vol. 128, no. 5, pp. 2898–2909, Nov. 2010.
[5] S. Liu, M. A. Khan, M. Bilal, and H. H. Zuberi, "Low probability detection constrained underwater acoustic communication: A comprehensive review," *IEEE Commun. Mag.*, vol. 63, no. 2, pp. 21–30, Feb. 2025.
[6] B. Sherlock, J. A. Neasham, and C. C. Tsimenidis, "Spread-spectrum techniques for bio-friendly underwater acoustic communications," *IEEE Access*, vol. 6, pp. 4506–4520, 2018.
[7] T. C. Yang and W.-B. Yang, "Performance analysis of direct-sequence spread-spectrum underwater acoustic communications with low signal-to-noise-ratio input signals," *J. Acoust. Soc. Amer.*, vol. 123, no. 2, pp. 842–855, Feb. 2008.
[8] T. C. Yang and W.-B. Yang, "Low probability of detection underwater acoustic communications for mobile platforms," in *Proc. OCEANS*, Sep. 2008, pp. 1–6.
[9] A. Song, M. Stojanovic, and M. Chitre, "Editorial underwater acoustic communications: Where we stand and what is next?" *IEEE J. Ocean. Eng.*, vol. 44, no. 1, pp. 1–6, Jan. 2019.
[10] Z. Li, M. Chitre, and M. Stojanovic, "Underwater acoustic communications review," *Nature Rev. Electr. Eng.*, vol. 2, no. 1, pp. 45–62, 2024.
[11] H. C. Song, W. S. Hodgkiss, W. A. Kuperman, W. J. Higley, K. Raghukumar, T. Akal, and M. Stevenson, "Spatial diversity in passive time reversal communications," *J. Acoust. Soc. Amer.*, vol. 120, no. 4, pp. 2067–2076, 2006.
[12] W. Hodgkiss and H. Song, "Time reversal experiments in the ocean," *J. Acoust. Soc. Amer.*, vol. 157, no. 4, p. 355, Apr. 2025.
[13] J. Gomes, A. Silva, and S. Jesus, "Adaptive spatial combining for passive time-reversed communications," *J. Acoust. Soc. Amer.*, vol. 124, no. 2, pp. 1038–1053, Aug. 2008.
[14] H.-C. Song, "An overview of underwater time-reversal communication," *IEEE J. Ocean. Eng.*, vol. 41, no. 3, pp. 644–655, Jul. 2016.
[15] M. Stojanovic, J. A. Catipovic, and J. G. Proakis, "Phase-coherent digital communications for underwater acoustic channels," *IEEE J. Ocean. Eng.*, vol. 19, no. 1, pp. 100–111, Jan. 1994.
[16] U. Vilaipornsawai, A. J. Silva, and S. M. Jesus, "Underwater communications for moving source using geometry-adapted time reversal and DFE: UAN10 data," in *Proc. OCEANS IEEE*, Jun. 2011, pp. 1–7.
[17] L. P. Maia, A. Silva, and S. M. Jesus, "Environmental model-based time-reversal underwater communications," *IEEE Access*, vol. 6, pp. 10041–10051, 2018.
[18] A. Lempel and M. Cohn, "On fast m-sequence transform," *IEEE Trans. Inf. Theory*, vol. IT-23, no. 1, pp. 135–137, Jan. 1977.
[19] F. B. Louza and H. A. DeFerrari, "Superimposed training low probability of detection underwater communications," *J. Acoust. Soc. Amer.*, vol. 148, no. 3, pp. 273–278, Sep. 2020.
[20] F. B. Louza, J. Osowsky, F. C. Xavier, E. E. Vale, L. P. Maia, R. P. Vio, M. V. S. Simões, V. Barroso, and S. M. Jesus, "Communications and biological monitoring experiment in an upwelling environment at cabo frio island bay," in *Proc. OCEANS*, Jun. 2019, pp. 1–7.
[21] T. C. Yang and W.-B. Yang, "Interference suppression for code-division multiple-access communications in an underwater acoustic channel," *J. Acoust. Soc. Amer.*, vol. 126, no. 1, pp. 220–228, Jul. 2009.
[22] R. Carvajal, K. Mahata, and J. C. Aguero, "Low complexity Wiener filtering in CDMA systems using a class of pseudo-noise spreading codes," *IEEE Commun. Lett.*, vol. 16, no. 9, pp. 1357–1360, Sep. 2012.
[23] C. B. Ribeiro, M. L. R. de Campos, and P. S. R. Diniz, "A new approach for channel equalization using Wiener filtering," in *Proc. GLOBECOM IEEE Global Telecommun. Conf.*, Nov. 2001, pp. 290–294.
[24] T. C. Yang, "Temporal resolutions of time-reversal and passive-phase conjugation for underwater acoustic communications," *IEEE J. Ocean. Eng.*, vol. 28, no. 2, pp. 229–245, Apr. 2003.
[25] H. S. Chang, "Detection of weak, broadband signals under doppler-scaled, multipath propagation," Ph.D. thesis, Dept. Elect. Eng. Comput. Sci., Univ. Michigan, 1992.
[26] A. Mahmood, M. Chitre, and H. Vishnu, "Locally optimal inspired detection in snapping shrimp noise," *IEEE J. Ocean. Eng.*, vol. 42, no. 4, pp. 1049–1068, Oct. 2017.
[27] C. E. L. Ferreira, J. E. A. Goncçalves, and R. Coutinho, "Community structure of fishes and habitat complexity on a tropical rocky shore," *Environ. Biol. Fishes*, vol. 61, no. 4, pp. 353–369, Aug. 2001.
[28] L. Calado, O. C. Rodríguez, G. Codato, and F. Xavier, "Upwelling regime off the cabo frio region in Brazil and impact on acoustic propagation," *J. Acoust. Soc. Amer.*, vol. 143, no. 3, pp. 174–180, Mar. 2018.
[29] F. B. Louza and S. M. Jesus, "The effects of upwelling over low SNR communications in shallow water," in *Proc. OCEANS*, Sep. 2021, pp. 1–6.
[30] R. K. R. Yarlagadda and J. E. Hershey, *Hadamard Matrix Analysis and Synthesis With Applications to Communications and Signal/Image Processing*. New York, NY, USA: Springer, 1997.

FÁBIO B. LOUZA received the M.Sc. degree in applied marine physics from the University of Miami, FL, USA, in 2016, and the Ph.D. degree in electrical and telecommunications engineering from the University of Algarve, Faro, Portugal, in 2022. He was an Officer with Brazilian Navy for nearly 27 years, gaining extensive experience in hydrographic and oceanographic operations aboard research vessels. His fieldwork includes surveys in the Amazon River basin and support for polar missions in Antarctica, contributing to oceanographic and acoustic research. He is currently the Head of the Underwater Acoustic Communications Division, Brazilian Navy Institute of Sea Studies Admiral Paulo Moreira (IEAPM). His research interests include acoustic propagation in fluvial and polar environments, low-probability-of-detection underwater acoustic communications, array signal processing, and acoustic vector sensors.

SÉRGIO M. JESUS (Member, IEEE) received the Doctorat Es-Sciences degree in engineering sciences from the Université de Nice, Nice, France, in 1986. From 1986 to 1992, he was a Staff Scientist with the SACLANT Undersea Research Centre, Ambient Noise and Signal Processing Group, La Spezia, Italy. During that period, he was involved with underwater acoustic field noise directionality and early studies on target detection using matched field processing. In 1992, he joined the Department of the Electrical Engineering and Computer Science, University of Algarve, Faro, Portugal, where he is currently a Full Professor. He has participated in 15 EU projects, five of which under his coordination. His research interests include underwater acoustics array signal processing, model-based inversion, ocean and seafloor tomography, underwater acoustic communications, and ocean noise. He is a member of the IEEE Signal Processing Society and the Acoustical Society of America.

Coordenação de Aperfeiçoamento de Pessoal de Nível Superior (CAPES) - ROR identifier: 00x0ma614